Spray Impact Resistance of a Superhydrophobic Nanocomposite Coating

Alexander Davis
Dept. of Mechanical and Aerospace Engineering, University of Virginia, Charlottesville, VA 22904

Smart Materials, Istituto Italiano di Tecnologia, Genoa 16163 Italy

Yong Han Yeong, Adam Steele, and Eric Loth
Dept. of Mechanical and Aerospace Engineering, University of Virginia, Charlottesville, VA 22904

Ilker S. Bayer
Dept. of Mechanical and Aerospace Engineering, University of Virginia, Charlottesville, VA 22904

Smart Materials, Istituto Italiano di Tecnologia, Genoa 16163 Italy

DOI 10.1002/aic.14457

The performance of a polyurethane/organoclay superhydrophobic nanocomposite modified with perfluoroalkyl methacrylic copolymer in the presence of a high-pressure air-water spray which mimics an icing cloud impact is investigated in this study. To quantify the average velocites of droplets impacting the superhydrophobic samples, a computational study was performed. Such a study is important to understand the interaction between the jet and surface. Impacting velocities for three different testing conditions were estimated to be 14.5, 4.5, and 3.4 m/s. Liquid saturation did not occur immediately, but over time, the high mass flow rate of water led to antiwetting performance degradation. Upon evaporation, contact angle returned to pretest values, indicating little mechanical erosion. This was consistent with scanning electron microscopy which showed that the nano and microstructure was preserved, and with energy-dispersive X-ray spectroscopy, which showed no surface chemistry change after testing. However, sliding angle showed stronger degradation, especially at higher impact velocities. © 2014 American Institute of Chemical Engineers *AIChE J*, 60: 3025–3032, 2014
Keywords: nanoclay, durability, spray impact

Introduction

Up to 50% of a wind turbine's annual power production can be lost due to inefficiencies caused by icing.[1] A promising way to alleviate this problem is through the use of antiwetting coatings. Inspired by lotus leaves, recent novel techniques combine microscale and nanoscale surface structure with low surface energy to create superhydrophobic synthetic surfaces (contact angle greater than 150° and sliding angle less than 10°).[2–5] These techniques include template synthesis, pulse electron deposition, electrochemical deposition, crystallization control, plasma treatment, Langmuir–Blodgett deposition, nanotube arrays, electro-spinning, and chemical vapor deposition.[6–9] Most of these techniques require some combination of vacuum processing (e.g., plasma treatment) and expensive or restricting fabrication tools which limit application to surfaces on the order of square centimeters. Thus, for large-scale industrial applications, low-cost spray-coated superhydrophobic nanocomposite surfaces may be the ideal solution.[10–15]

The mechanical durability and preservation of antiwetting performance when subjected to mechanical abrasion has been explored for several types of superhydrophobic surfaces.[16] Steele et al.[17] found that contact angles above 160° and contact angle hysteresis below 10° was maintained for a polyurethane/organoclay nanocomposite when subjected to a 1750 N/m adhesion strength tape test, and a 3850 N/m test did not noticeably remove any coating. A superamphiphobic surface was recently made from fluorosurfactant-modified silica aerogel that stayed superamphiphobic when rubbed 100 times with 600 grit sandpaper under 450 Pa pressure.[18] Superhydrophobicity of micromolded polypropylene remained intact when pressed with 500 kPa pressure.[19] When tested under 32 kPa linear abrasion, polyethylene sheets that had been laminated over steel mesh remained superhydrophobic for over 5500 cycles.[20]

A major challenge for these superhydrophobic coatings is the ability to perform under droplet impact. This is especially a concern for the increasing number of wind turbines being constructed offshore. One source of droplet impact on a wind turbine blade is impacting fog droplets. Droplet impact could cause erosion of the superhydrophobic coating's surface structure, reducing performance. Another danger of droplet impact is it could, even without mechanically wearing the surface, cause a transition from the nonwetting Cassie state to the wetting Wenzel state. This transition, known herein as "saturation," occurs when it becomes thermodynamically favorable for the asperities on a

---

Correspondence concerning this article should be addressed to A. Davis at alexander.davis@iit.it.

superhydrophobic surface to become penetrated with water.[21] Saturation has been induced in the past through the application of force or pressure to the droplet,[22] electric voltage,[23,24] light for a photocatylitic texture,[25] and vibration.[26] Other studies have investigated this transition when it is caused by prolonged liquid contact.[27–30]

There are very few studies of jets impacting superhydrophobic surfaces, with most work done in the past limited to studying the low velocity impact and immediate rebound of single ~1-mm diameter droplets.[31–36] However, to date, investigations have been limited to single droplets where no erosion is expected, and thus, were not indicative of an environment in which a wind turbine operates. This experimental study investigates the performance of a novel polyurethane/organoclay superhydrophobic nanocomposite coating against a high-pressure air-water spray to simulate fog impact. Superhydrophobic samples were impacted with an air jet laden with droplets representative of an icing cloud at three different impacting velocities. A computational fluid dynamics (CFD) study was performed to find the velocities of the impacting droplets. The antiwetting performance was examined immediately after spraying intervals as well as after water trapped in the textured surfaces was allowed to evaporate.

Experimental

Sample preparation

The process for sample preparation was the same as used by Steele et al.[17] Precursor solutions were first created, followed by spray casting and then thermosetting to produce the final nanocomposite coatings. Alcohols are common solvents for epoxy and polyurethane formulations. A recent study found that alcohols can have a strong tendency to adsorb on layered silicate surfaces rendering the surfaces functional for many applications including polymer reinforcement.[37] Thus, as-received dimethyl dialkyl C14-C18 amine functionalized montmorillonite clay particles (Nanoclay, Nanocor) were first dispersed in ethyl alcohol at room temperature and then waterborne perfluoroalkyl methacrylic copolymer (PMC; 30% wt polymer, 70% wt water; Dupont) was added slowly to the solution and blended with vortex mixing. Fluorinated polymers are of interest due to their extremely low surface energies, while an organoclay-based nanocomposite coating is desirable because it is both compatible with fluoroacrylics and environmentally friendly unlike some other nanofiller materials, for example, carbon nanotubes.[38–40] Separately, moisture cured polyurethane (MCPU) was also dispersed in ethyl alcohol. The MCPU (Gorilla Glue) was a one-component liquid formula comprising 25% diphenylmethane-diisocyanate and 75% polyurethane prepolymer (hexanedioic acid, polymer with 1,6-hexanediol and 1,1-methylenebis 4-isocyanatobenzene). Its viscosity was measured to be 4200 mPa s at 25°C. This type of polyurethane formula is commonly found in many commercially available adhesives such as Titebond and Gorilla. Finally, the alcohol/organoclay/PMC suspension was blended into the MCPU solution, creating a Pickering emulsion. The final blend was stirred using a vortex mixer for 15 min until the mixture was in a homogenous and stable state.

The ethyl alcohol solvent concentration can also be tailored to suit the spray applicator if necessary to obtain a "dry" spray coating and counteract the coffee stain effect.[41] To create the nanocomposite coatings from this precursor solution, the slurries were spray cast onto aluminum substrates using an internal mix, double-action airbrush atomizer (model VL-SET, Paasche). The substrates were coated with a single spray application and then heat cured at 100°C overnight.

Spray test setup

The test design was centered around a set of MOD-1 air-assist nozzles supplied by the NASA Glenn Research Center Icing Research Tunnel (IRT). These nozzles were chosen because of their well-known correlation between inlet air and water pressures and resulting droplet sizes produced. The nozzles were also desirable because of the extensive work done in the past by Bulzan et al.[42] to both numerically and experimentally validate the nozzle's radial and axial profiles of velocity and turbulent kinetic energy.

The test setup consisted of a MOD-1 nozzle pointed vertically down toward a test sample. The nozzle was enclosed inside of a brass adapter with inlets for water and air. The design of the nozzle and adapter allowed for the distinct air-water mixtures to be created. Tap water entered the adapter from the back inlet and flowed unubstructed through the nozzle. Air entered the adapter from the side inlet and into a cavity around the nozzle. The air could then circulate freely around the nozzle and enter the stream through a series of holes drilled around the outer surface of the nozzle. The nozzle had an exit 0.935 cm in diameter. Unlike other air-assist nozzles, it did not use swirling for atomization. The adapter had extensions on either side with screw holes. These extensions were attached to stationary aluminum struts on either side with mounting holes 5 cm apart and allowed for a maximum of 65 cm of distance between the nozzle and the superhydrophobic sample. The sample was mounted on a lab jack that allows for micrometer height adjustments that total less than 2.5 cm. A schematic of the setup is shown in Figure 1.

The nozzle was supplied with a water pressure of 50 psi and air pressure 20 psi to create a spray of 20 μm mean volume diameter (MVD) droplets. The air and water mass flow rates were approximately 2.3 and 0.5 g/s, respectively.[42] For three different test runs, the nozzle was placed at distances of 25, 45, and 65 cm from the superhydrophobic sample. The upper limit of 65 cm was chosen because it was the largest distance possible in the spray test setup. The lower limit of 25 cm was chosen to ensure that droplet atomization was complete after exiting the MOD-1 nozzle.

A sample was made for each of the spray distances. Droplets were sprayed onto each sample in 10 s time intervals. After each spray interval, the sample was shaken by hand for 2 min to clear any large droplets from the surface. Compressed air was then blown on the surface for 10 s from a distance of approximately 3 in. to clear off remaining droplets. A CMOS camera (Canon T2i, Canon) with a macro lens (MP-E 65mm f/2.8 1–5xm Canon) was used to capture static and dynamic water droplet images on a custom tilt stage for wettability measurements. ImageJ was then used to process the images with a Java plugin (Drop Shape Analysis, Aurlien Stalder)[43] to calculate the static and dynamic contact angles. Contact angles were measured at three different points on the surface after each spray interval, with the average reported. After 5 time intervals, equaling a total of 50 s, the sample was heated at 100°C for 30 min to evaporate any water trapped inside the surface asperities. Scanning electron micrographs (SEM) were taken of superhydrophobic samples

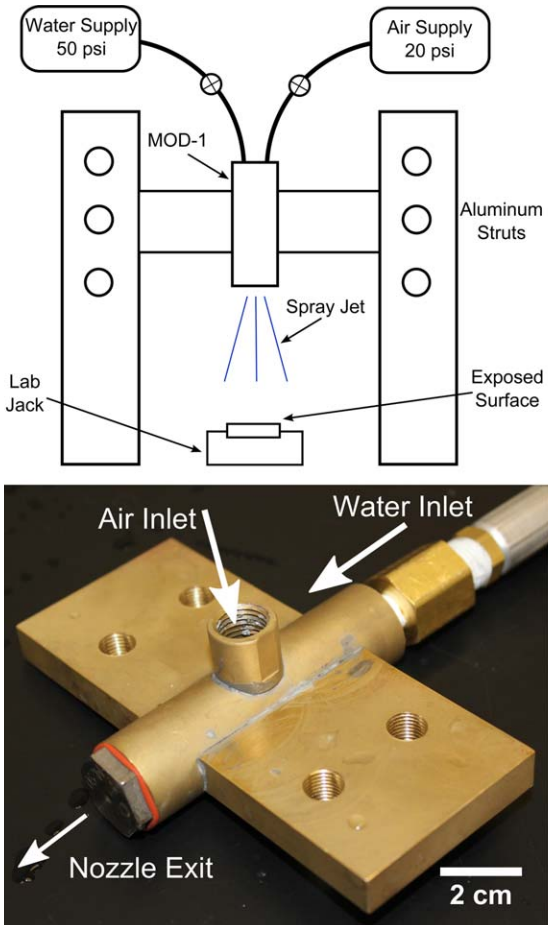

Figure 1. Top, a schematic of spray test setup to investigate superhydrophobic surface saturation and bottom, photo of MOD-1 nozzle inside adapter.

[Color figure can be viewed in the online issue, which is available at wileyonlinelibrary.com.]

after being sprayed from 45 to 65 cm to compare surface morphology before and after testing. Energy-dispersive X-ray spectroscopy (EDXS) was also performed before and after testing using a PGT IMIX-SPIRIT detector.

Computational Modeling

To estimate the velocities of impacting droplets, numerical predictions were obtained from a density-based Reynolds Average Navier-Stokes (RANS) approach using the FLUENT software package. The temporal discretization of the RANS equations used a second-order upwind scheme for the momentum, turbulence, and dissipation conservation equations. The two equation k-ω Menter-SST was chosen for the turbulence model. The mesh used was 2-D, axisymmetric, and contained about 16,000 nodes. The same discretization scheme, governing equations, and turbulence model for free jet calculations (i.e., without a downstream wall) were utilized by Clark and Loth, who also investigated the effect of grid resolution on convergence.[44] Mass flow was assumed to be choked at the nozzle exit, with a Mach number equal to 1. CFD was first used to find the downstream characteristics of pure airflow coming from a MOD-1 nozzle with no obstructions downstream. An injection of water droplets was then released 10 cm from the nozzle exit. The initial droplet velocities were set to the axial velocities found experimentally by Bulzan et al.[42] at this downstream distance from the nozzle exit. Experimental data were found using a two-component phase/Doppler instrument.

The water droplet sizes were based off of a cumulative distribution function tabulated from experimental data[45] obtained within the NASA Glenn IRT. The experimental data had a range of water droplet sizes with a MVD of 21 μm. The experimental data were fitted with a Rosin-Rammler distribution using the equation below

$$C(d)=1-\exp\left[-\left(\frac{d}{d_{rr}}\right)^{\frac{1}{h_{rr}}}\right]$$

In this expression, $C(d)$ is the cumulative droplet distribution, d is the droplet diameter, d_{rr} is the reference diameter and corresponds to $C(d) = 0.63$, and h_{rr} is the spread parameter. For the current Rosin-Rammler fit, $d_{rr} = 24$ μm and $h_{rr} = 2.4$. This cumulative distribution function was converted into a probability density function and 10 droplet bin sizes were determined by keeping the integral of the Rosin-Rammler fit equal between each droplet size which can be seen by the black lines in Figure 2. Ten different droplet diameters were chosen to give an adequate range of droplet sizes and using the Rosin-Rammler fit allows the MVD to stay at 21 μm and to match with experiments.

The droplet trajectories were computed with a Lagrangian discrete-phase model with a particle time step of 100 μs. For improvement in the predictive ability of turbulent droplet diffusion, a Discrete Random Walk (DRW) model was used. In the DRW model, a Gaussian random number generator is used to describe instantaneous fluid velocity perturbation so that information for the mean particle diffusion can be subsequently obtained. The droplet force-balance equation implemented a sphere drag law[46] but neglected lift forces, droplet-droplet interactions, and droplet break-up. The airflow was analyzed from simulations with droplets with two way coupling. The cases of a wall 25, 45, and 65 cm from the nozzle exit were then investigated. A stationary wall with a no-slip boundary condition was placed at these downstream distances. Trajectory calculations of droplets were set to terminate if they came into contact with the wall. A sample of droplets was taken at the downstream wall to find the axial velocities upon impact.

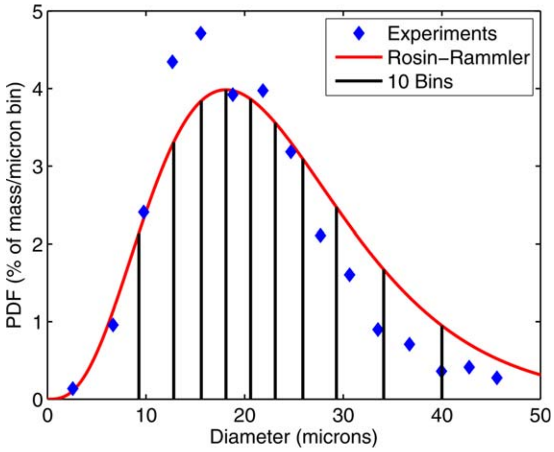

Figure 2. Distribution of droplet size bins used in computational study.

[Color figure can be viewed in the online issue, which is available at wileyonlinelibrary.com.]

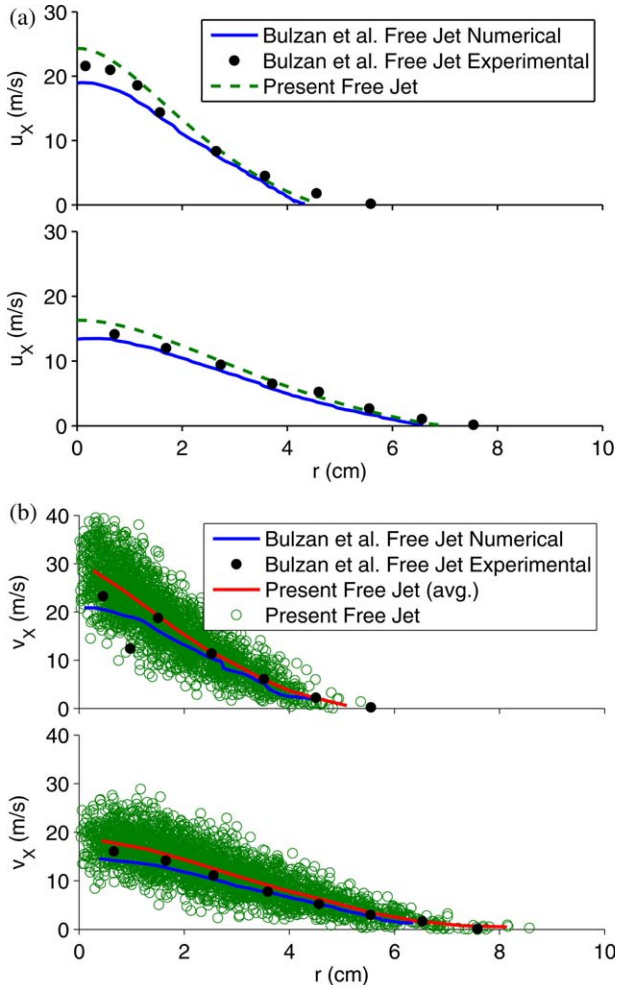

Figure 3. Radial flow characteristics for (a) gas phase and (b) droplet phase.

[Color figure can be viewed in the online issue, which is available at wileyonlinelibrary.com.]

Results and Discussion

Computational results

Figure 3 shows the flow characteristics of an unobstructed free jet exiting the MOD-1 nozzle determined by the current study along with a comparison to Bulzan's previous study.[42] Figures 3a, b show the radial variation of u_x, defined as gas-phase axial velocity, and v_x, defined as droplet axial velocity, at distances of 20 and 30 cm downstream of the nozzle exit. For both phases and downstream distances, the present computational study gives higher axial velocities than Bulzan's, but more closely matches Bulzan's experiments, indicating the present computational results can be used to predict experimental results. u_x reaches a velocity of about 25 m/s at the centerline 20 cm downstream of the nozzle exit, and tapers off to zero at a radial distance of 4 cm from the centerline. At 30 cm downstream of the nozzle, u_x is 16 m/s at the centerline, and positive velocity is found up to 7 cm away from the centerline. v_x values are slightly higher than u_x values at 20 cm from the nozzle, but the two more closely match at 30 cm. Figure 4 shows the axial variation of $u_{x,\mathrm{CL}}$ (defined as gas-phase axial velocity along the jet centerline) for the present free jet and comparison to Bulzan et al. Also shown are the axial velocities in the cases of an impinging wall. Once again, the axial velocities from the present study are higher than Bulzan found numerically, but match Bulzan's experimental results. In the cases of an impinging wall, u_x decelerates to 0 m/s at the wall as is required. As the impinging wall moves closer to the nozzle exit (i.e., from 65 to 25 cm), the deceleration of the jet to zero occurs closer to the wall. For example, when the wall is 65 cm from the nozzle exit deceleration starts about 10 cm upstream of the wall. Whereas when the wall is 25 cm from the exit, deceleration starts about 6 cm ahead of the wall.

Figure 5 shows a scatter plot of droplets downstream of the MOD-1 nozzle in all three wall cases, as well as the axial velocities of the droplets as they impact, $v_{x,\mathrm{impact}}$. As mentioned above, droplets were injected 10 cm downstream of the nozzle exit. In the cases of walls 45 and 65 cm downstream, $v_{x,\mathrm{impact}}$ tend to $u_{x,\mathrm{CL}}$ at those downstream distances, shown in a dashed gray line. However, for a 25 cm downstream wall, some impacting droplets have a higher axial velocity than $u_{x,\mathrm{CL}}$ at that distance. Bulzan et al. also found that droplets have higher velocities than the gas phase through the first ∼30 cm. Figure 6 shows the average $v_{x,\mathrm{impact}}$ within 2.5 cm of the centerline, corresponding to the area that a superhydrophobic sample would be exposed to during testing. Also shown is "Impact %," defined as the fraction of droplets that impact within 2.5 cm of the centerline. Average $v_{x,\mathrm{impact}}$ decreases from 14.5 m/s at 25 cm, to 4.5 m/s at 45 cm, to 3.4 m/s at 65 cm. For a total number of 1500 droplets sampled in each case, Impact % also decreases as wall distance increases. Impact % decreases from 46% at 25 cm, to 19% at 45 cm, to 7 % at 65 cm.

Experimental results

Figure 7 shows the effect of droplet impact on the contact angle of each superhydrophobic sample immediately after each spraying interval. Before spraying, each of the samples produced a contact angle of 150 ± 2°. All three samples lost about the same amount of performance after being sprayed for 10 s. After that point, the difference in impacting velocities became clear. While the 65 and 45 cm samples again lost some performance after 30 s, the 25 cm sample saw a substantial loss in contact angle. At the conclusion of spraying at 50 s, the 65 and 45 cm samples produced a contact angle measurement of 99° and 94°, respectively, while the

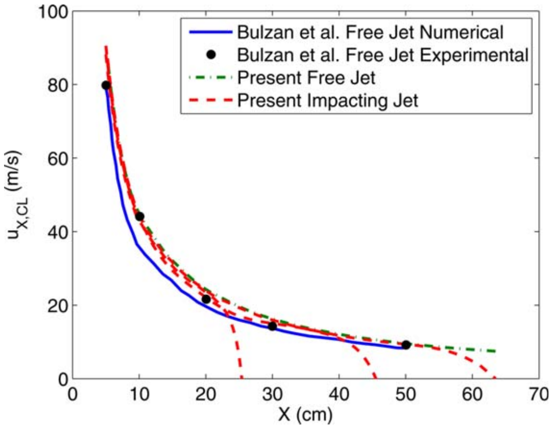

Figure 4. Axial variation of gas-phase centerline axial velocity.

[Color figure can be viewed in the online issue, which is available at wileyonlinelibrary.com.]

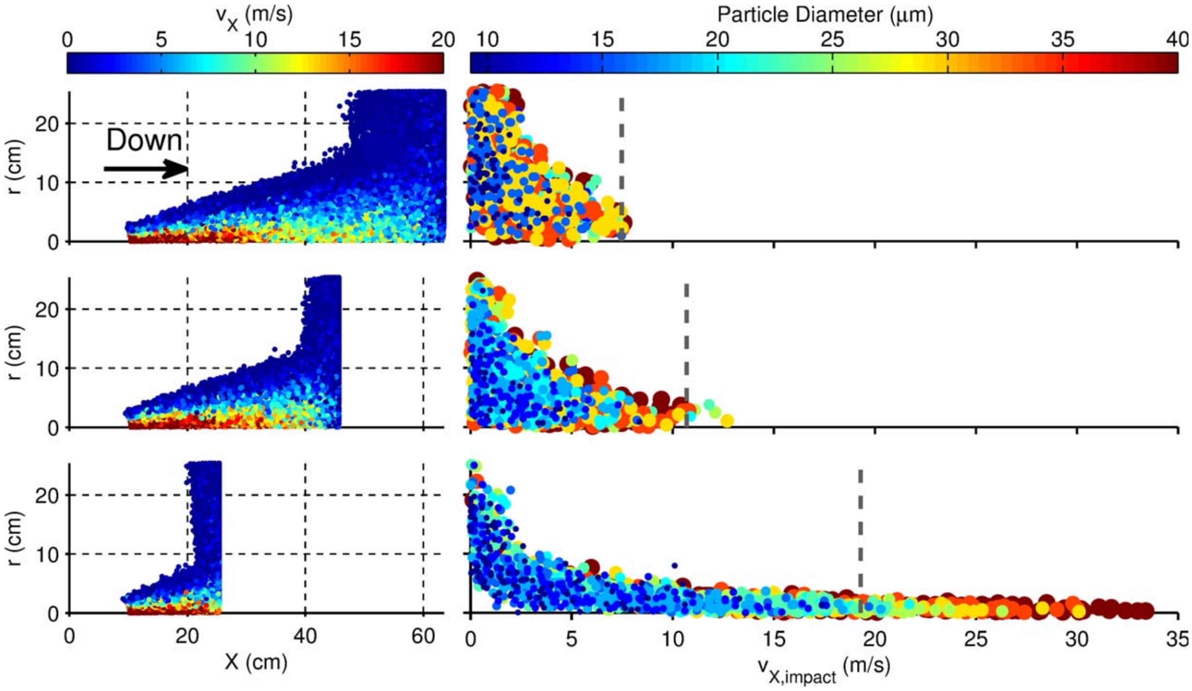

Figure 5. Scatter plot of droplets (colored by axial velocity) and axial velocity of impacting droplets (colored by droplet size) for a wall 65 cm (top), 45 cm (middle), and 25 cm (bottom) away from nozzle exit.

Freejet gas-phase axial velocity at those downstream distances are shown in a dashed gray line. [Color figure can be viewed in the online issue, which is available at wileyonlinelibrary.com.]

25 cm sample produced a contact angle of 70°. Upon heating the samples after spraying, the contact angle for each sample returned to its original value. This suggests that the loss in performance during spraying was not due to mechanical erosion or a change in surface morphology, but rather due to liquid saturation of the microtextured surface. This saturation effectively changed the surface from the superhydrophobic Cassie state to the wetted Wenzel state. Once the liquid was allowed to evaporate from the asperities on the surface, the nonwetting performance returned.

Saturation most likely originated from two sources. First, as can be seen in Figure 8, the distance between large asperities on the surface can be as large as 50–100 μm. This is enough space for individual droplets to penetrate the microasperities. Second, as is noted by Deng et al.,[34] the stagnation pressure of impacting droplets was likely large enough to overpower the capillary pressure of the asperities, causing droplets to penetrate the microtexture. The hypothesis that no mechanical erosion occurred and that all loss in performance was due to saturation is supported by the SEM images shown in Figure 8. While differences can be seen when comparing surface morphologies before and after 45 and 25 cm impact, these differences are typical of variations seen when examining different locations on the same irregular surface.

The performance of the samples before spraying and after surface moisture evaporation is shown in Figure 9. It was clear that contact angle (Figure 9a) was unaffected by the droplet impact, as these values returned to their original state after each of the samples was dried. However, sliding angles (Figure 9b) increased significantly for the highest impact velocity even after water was allowed to evaporate. One possible cause of this increase involves recognizing that contact angle and sliding angle are not necessarily coupled. For example, an improvement in contact angle does not necessarily bring an improvement in sliding angle. It has been shown that increased roughness, which is critical for an increased contact angle and superhydrophobicity in general, can actually lead to a higher sliding angle.[47] EDXS, shown in Figure 10, did not reveal a change in surface chemistry. Carbon and fluorine (components of PMC) and aluminum, silicon, and titanium (components of montmorillonite clay) were all detected as much before testing as after. It is important to note that EDXS detects elements in the bulk of a tested sample, several microns within the surface. Thus, a change in the surface chemistry of the superhydrophobic sample might not have been detected. Another possible reason for the degradation in sliding angle is that the fluoropolymer chains present on the surface restructured while being exposed to water for extended periods of time. A monolayer

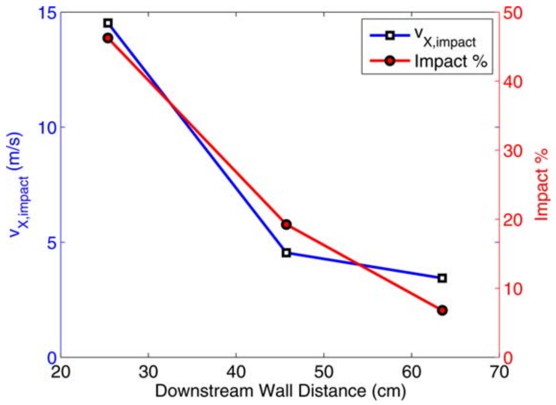

Figure 6. Average droplet impact velocity and fraction of all impacting droplets that impact within a 2.5 cm of the centerline as a function of downstream wall distance.

[Color figure can be viewed in the online issue, which is available at wileyonlinelibrary.com.]

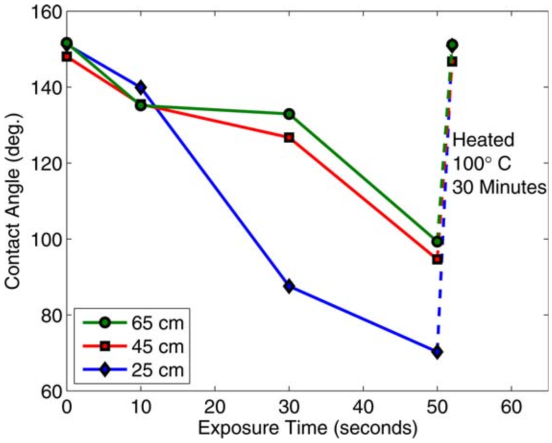

Figure 7. Variation of contact angle with spray time for different spray distances.

Each data point represents the average of three measurements, for which the average variation was approximately 10°. Such high variability is not uncommon for stochastic surfaces, particularly ones that have gone through some sort of chemical or mechanical durability test.[19,50,51] [Color figure can be viewed in the online issue, which is available at wileyonlinelibrary.com.]

of the cationic surfactant dimethyl-dioctadecyl-ammonium bromide on mica was found to rearrange into a patchy bilayer when immersed underwater for 90 min, covering only 60% of the area it had before immersion.[48] Molecular dynamics simulations predicted that a monolayer of surfactant with a 24 carbon chain remained intact when immersed underwater, but one with an 18 carbon chain restructured into spherical micelles with hydrophilic head groups oriented toward water.[49] PMC complies with the PFOA Stewardship Program and consists of a six carbon chain. A change in the orientation of the polymer would not have been detected

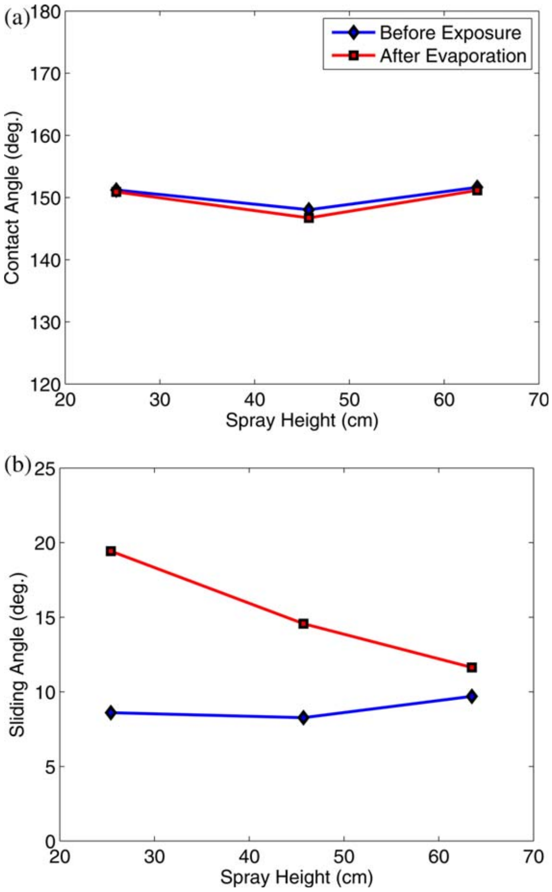

Figure 9. (a) Contact angle and (b) sliding angle of samples before spray tests and after surface moisture evaporation.

[Color figure can be viewed in the online issue, which is available at wileyonlinelibrary.com.]

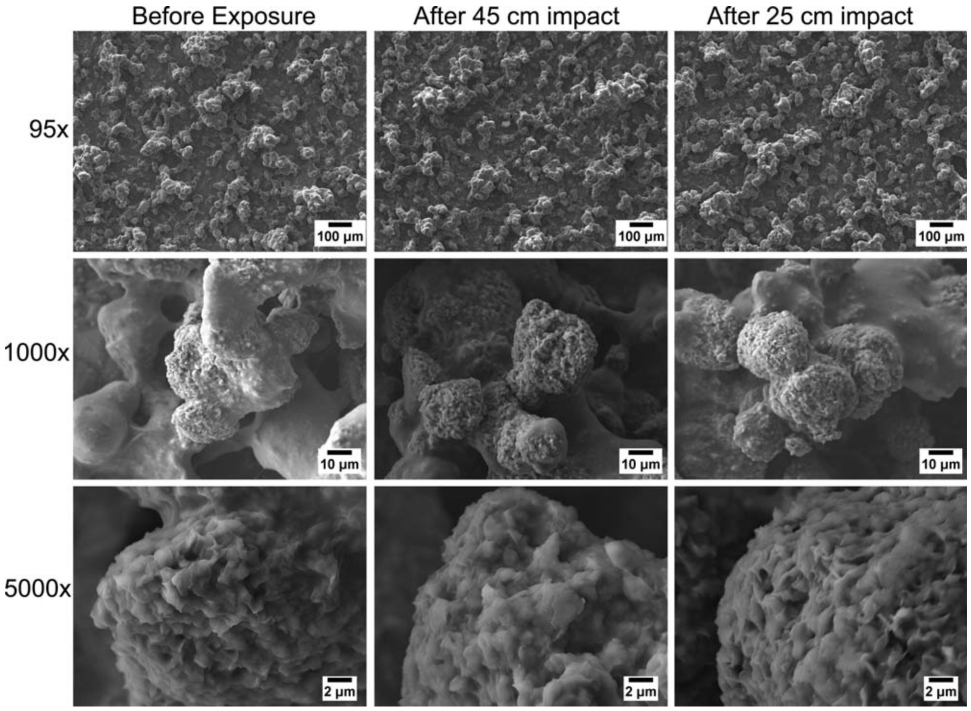

Figure 8. SEM images of superhydrophobic surface before testing and after testing.

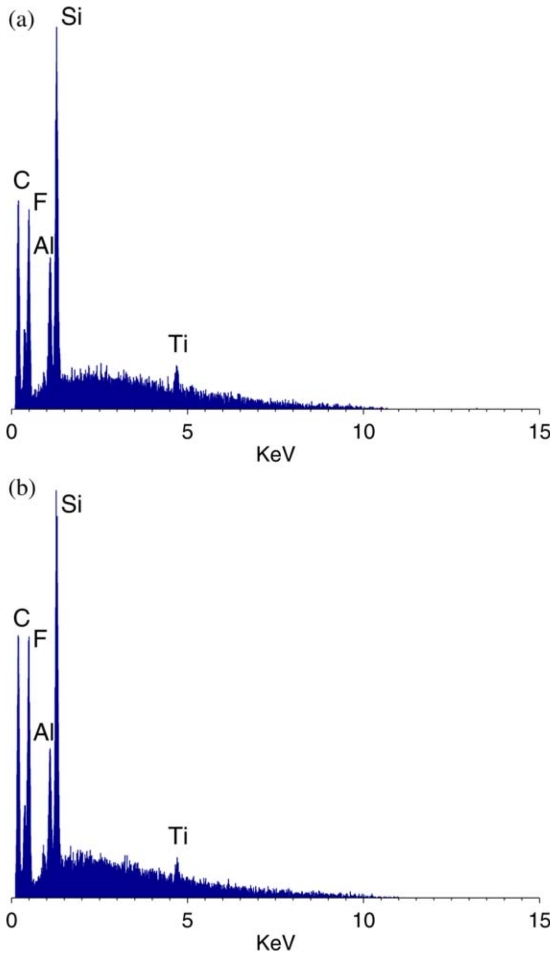

Figure 10. EDXS of superhydrophobic samples (a) before testing and (b) after 25 cm spray impact

[Color figure can be viewed in the online issue, which is available at wileyonlinelibrary.com.]

through EDXS. Elements present in tap water used in the experiment might have also contaminated the surface.

Conclusions

In this experimental study, polyurethane/organoclay superhydrophobic nanocomposite-coated aluminum samples were sprayed with 25 μm droplets impacting at 25, 45, and 65 cm to simulate fog droplet impact. It was shown that antiwetting performance degraded as a function of spray time and impact velocity. Contact angle returned to pretest values after the water that had penetrated the surface's microtexture was allowed to evaporate. However, sliding angle increased with increasing droplet impact velocity. Maintaining mechanical structure while being impacted with fog-sized droplets is an important step in bringing superhydrophobic nanocomposites to real world use. Based on the results of this study, future work will include increasing the size of impacting droplets to simulate rain impact, performing further CFD calculations to find the relationship between wall distance and average impact velocity, as well as tailoring nanocomposite surfaces to improve saturation resistance to such conditions.

Literature Cited

1. Parent O, Ilinca A. Anti-icing and de-icing techniques for wind turbines: critical review. *Cold Reg Sci Technol.* 2011;65:88–96.
2. Li XM, Reinhoudt D, Crego-Calama M. What do we need for a superhydrophobic surface? A review on the recent progress in the preparation of superhydrophobic surfaces. *Chem Soc Rev.* 2007;36:1350–1368.
3. Roach P, Shirtcliffe NJ, Newton MI. Progess in superhydrophobic surface development. *Soft Matter.* 2008;4:224–240.
4. Yan Y, Gao N, Barthlott W. Mimicking natural superhydrophobic surfaces and grasping the wetting process: a review on recent progress in preparing superhydrophobic surfaces. *Adv Colloid Interface Sci.* 2011;169:80–105.
5. Xue CH, Ma JZ. Long-lived superhydrophobic surfaces. *J Mater Chem A.* 2013;1:4146–4161.
6. Feng X, Jiang L. Design and creation of superwetting/antiwetting surfaces. *Adv Mater.* 2006;18:3063–3078.
7. Shirtcliffe NJ, McHale G, Newton MI. The superhydrophobicity of polymer surfaces: recent developments. *J Polym Sci Part B Polym Phys.* 2011;49:1203–1217.
8. Xue Z, Liu M, Jiang L. Recent developments in polymeric superoleophobic surfaces. *J Polym Sci Part B Polym Phys.* 2012;50:1209–1224.
9. Im SG, Gleason KK. Solvent-free modification of surfaces with polymers: the case for initiated and oxidative chemical vapor deposition (CVD). *AIChE J.* 2011;57:276–285.
10. Schutzius TM, Bayer IS, Jursich GM, Das A, Megaridis CM. Superhydrophobic-superhydrophilic binary micropatterns by localized thermal treatment of polyhedral oligomeric silsesquioxane (POSS)-silica films. *Nanoscale.* 2012;4:5378–5385.
11. Bayer IS, Caramia V, Fragouli D, Spano F, Cingolani R, Athanassiou A. Electrically conductive and high temperature resistant superhydrophobic composite films from colloidal graphite. *J Mater Chem.* 2012;22:2057–2062.
12. Bayer IS, Fragouli D, Martorana PJ, Martiradonna L, Cingolani R, Athanassiou A. Solvent resistant superhydrophobic films from self-emulsifying carnauba wax-alcohol emulsions. *Soft Matter.* 2011;7:7939–7943.
13. Schutzius TM, Bayer IS, Tiwari MK, Megaridis CM. Novel fluoropolymer blends for the fabrication of sprayable multifunctional superhydrophobic nanostructured composites. *Ind Eng Chem Res.* 2011;50:11117–11123.
14. Yeong YH, Steele A, Loth E, Bayer I, Combarieu GD, Lakeman C. Temperature and humidity effects on superhydrophobicity of nanocomposite coatings. *Appl Phys Lett.* 2012;100:053112.
15. Schutzius TM, Tiwari MK, Bayer IS, Megaridis CM. High strain sustaining, nitrile rubber based, large-area, superhydrophobic, nanostructured composite coatings. *Compos A.* 2011;42:979–985.
16. Bayer IS, Brown A, Steele A, Loth E. Transforming anaerobic adhesives into highly durable and abrasion resistant superhydrophobic organoclay nanocomposite films: a new hybrid spray adhesive for tough superhydrophobicity. *Appl Phys Express.* 2009;2:125003.
17. Steele A, Bayer I, Loth E. Adhesion strength and superhydrophobicity of polyurethane/organoclay nanocomposite coatings. *J Appl Polym Sci.* 2012;125:E445–E452.
18. Jin H, Tian X, Ikkala O, Ras RHA. Preservation of superhydrophobic and superoleophobic properties upon wear damage. *ACS Appl Mater Interfaces.* 2013;5:485–488.
19. Huovinen E, Hirvi J, Suvanto M, Pakkanen TA. Micromicro hierarchy replacing micronano hierarchy: a precisely controlled way to produce wear-resistant superhydrophobic polymer surfaces. *Langmuir.* 2012;28:14747–14755.
20. Xu QF, Mondal B, Lyons AM. Fabricating superhydrophobic polymer surfaces with excellent abrasion resistance by a simple lamination templating method. *ACS Appl Mater Interfaces.* 2011;3:3508–3514.
21. Bico J, Thiele U, Qur D. Wetting of textured surfaces. *Colloids Surf A.* 2002;206:41–46.
22. Lafuma A, Quéré D. Superhydrophobic states. *Nat Mater.* 2003;2:457–460.
23. Bahadur V, Garimella SV. Electrowetting-based control of static droplet states on rough surfaces. *Langmuir.* 2007;23:4918–4924.
24. Krupenkin TN, Taylor JA, Schneider TM, Yang S. From rolling ball to complete wetting: the dynamic tuning of liquids on nanostructured surfaces. *Langmuir.* 2004;20:3824–3827.
25. Feng X, Feng L, Jin M, Zhai J, Jiang L, Zhu D. Reversible superhydrophobicity to super-hydrophilicity transition of aligned ZnO nanorod films. *J Am Chem Soc.* 2004;126:62–63.
26. Bormashenko E, Pogreb R, Whyman G, Erlich M. CassieWenzel wetting transition in vibrating drops deposited on rough surfaces: is

the dynamic CassieWenzel wetting transition a 2D or 1D affair? *Langmuir*. 2007;23:6501–6503.

27. Wang S, Feng L, Jiang L. One-step solution-immersion process for the fabrication of stable bionic superhydrophobic surfaces. *Adv Mater*. 2006;18:767–770.
28. Nicolas M, Guittard F, Gribaldi S. Synthesis of stable super water- and oil-repellent polythiophene films. *Angew Chem*. 2006;118:2309–2312.
29. Zimmermann J, Artus GRJ, Seeger S. Long term studies on the chemical stability of a superhydrophobic silicone nanofilament coating. *Appl Surf Sci*. 2007;253:5972–5979.
30. Cheek J, Steele A, Bayer IS, Loth E. Underwater saturation resistance and electrolytic functionality for superhydrophobic nanocomposites. *Colloid Polym Sci*. 2013;291:2013–2016.
31. Tsai P, Pacheco S, Pirat C, Lefferts L, Lohse D. Drop kmpact upon micro- and nanostructured superhydrophobic surfaces. *Langmuir*. 2009;25:12293–12298.
32. Li X, Ma X, Lan Z. Behavioral patterns of drop impingement onto rigid substrates with a wide range of wettability and different surface temperatures. *AIChE J*. 2009;55:1983–1992.
33. Chiarot P, Jones T. Grazing impact of continuous droplet streams with a superhydrophobic surface. *Exp Fluids*. 2010;49:1109–1119.
34. Deng T, Varanasi KK, Hsu M, Bhate N, Keimel C, Stein J, Blohm M. Nonwetting of impinging droplets on textured surfaces. *Appl Phys Lett*. 2009;94(13):133109–133109–3.
35. Chen L, Xiao Z, Chan PCH, Lee YK, Li Z. A comparative study of droplet impact dynamics on a dual-scaled superhydrophobic surface and lotus leaf. *Appl Surf Sci*. 2011;257:8857–8863.
36. Bayer IS, Megaridis CM. Contact angle dynamics in droplets impacting on flat surfaces with different wetting characteristics. *J Fluid Mech*. 2006;558:415–449.
37. Kowalczyk K, Spychaj T. Epoxy coatings with modified montmorillonites. *Prog Org Coat*. 2008;62:425–429.
38. Ma M, Hill RM. Superhydrophobic surfaces. *Curr Opin Colloid Interface Sci*. 2006;11:193–202.
39. Bayer IS, Steele A, Martorana P, Loth E, Robinson SJ, Stevenson D. Biolubricant induced phase inversion and superhydrophobicity in rubber-toughened biopolymer/organoclay nanocomposites. *Appl Phys Lett*. 2009;95(6):063702.
40. Wang CF, Chen WY, Cheng HZ, Fu SL. Pressure-proof superhydrophobic films from flexible carbon nanotube/polymer coatings. *J Phys Chem C*. 2010;114:15607–15611.
41. Steele A, Bayer I, Loth E. Inherently superoleophobic nanocomposite coatings by spray atomization. *Nano Lett*. 2009;9:501–505.
42. Bulzan DL, Levy Y, Aggarwal S, Chitre S. Measurements and predictions of a liquid spray from an air-assist nozzle. *Atomization Sprays*. 1992;2:445–462.
43. Stalder AF, Kulik G, Sage D, Barbieri L, Hoffmann P. A snake-based approach to accurate determination of both contact points and contact angles. *Colloids Surf A*. 2006;286:92–103.
44. Clark KM, Loth E. A multi-scale LES technique for coupling near-field and far-field domains for a jet flow. *Comput Fluids*. 2013;88: 262–271.
45. Bhargava C, Loth E, Potapczuk M. Simulating the aerodynamics of the NASA John H. *Glenn icing research tunnel*. *J Aircr*. 2005;42: 671–684.
46. Morsi SA, Alexander AJ. An investigation of particle trajectories in two-phase flow systems. *J Fluid Mech*. 1972;55:193–208.
47. Miwa M, Nakajima A, Fujishima A, Hashimoto K, Watanabe T. Effects of the surface roughness on sliding angles of water droplets on superhydrophobic surfaces. *Langmuir*. 2000;16:5754–5760.
48. Meyer EE, Lin Q, Hassenkam T, Oroudjev E, Israelachvili JN. *Origin of the long-range attraction between surfactant-coated surfaces*. *PNAS* 2005;102:6839–6842.
49. Das J, Eun C, Perkin S, Berkowitz ML. Restructuring of hydrophobic surfaces created by surfactant adsorption to mica surfaces. *Langmuir*. 2011;27:11737–11741.
50. Deng B, Cai R, Yu Y, Jiang H, Wang C, Li J, Li L, Yu M, Li J, Xie L, Huang Q, Fan C. Laundering durability of superhydrophobic cotton fabric. *Adv Mater*. 2010;22(48):5473–5477.
51. Wang F, Lei S, Ou J, Xue M, Li W. Superhydrophobic surfaces with excellent mechanical durability and easy repairability. *Appl Surf Sci*. 2013;276:397–400.

Manuscript received Jun. 11, 2013, and revision received Feb. 14, 2014.